Available online at www.sciencedirect.com

ScienceDirect

Journal of the European Ceramic Society 30 (2010) 2533–2545

www.elsevier.com/locate/jeurceramsoc

Cr^{3+} microspectroscopy measurements and modelling of local variations in surface grinding stresses in polycrystalline alumina

Sheng Guo **, Richard I. Todd *

Department of Materials, Parks Road, University of Oxford, Oxford OX1 3PH, United Kingdom

Received 4 February 2010; received in revised form 1 April 2010; accepted 4 April 2010
Available online 9 June 2010

Abstract

Surface residual stresses caused by grinding and polishing of alumina are thought to influence materials properties but have previously been measured only by low spatial resolution techniques which sample average stresses. In this work confocal Cr^{3+} fluorescence microscopy has been used to investigate the spatial distribution of the residual stresses. A model for the residual stresses, accounting for both surface plastic deformation and "pullout" of material from the surface by brittle fracture, was developed to help in analysing the results. After coarse diamond grinding, the results showed that the residual stresses fluctuate greatly with position. Large tensile stresses (up to ~600 MPa) were found below the plastically deformed surface layer in regions between the "pullouts". These tensile stresses are expected to aid crack propagation and further surface pullout. They arise because pullout removes parts of the plastically deformed surface layer. The stresses beneath the pullout sites themselves were compressive, but the largest compressive stresses (≈−1.5 GPa) were within the plastically deformed surface regions and extended to a depth of 1.3 μm. The plastically deformed surface layer was much shallower following polishing with 3 μm diamond paste but the compressive stress within it was of similar magnitude to that in the plastically deformed surface layer caused by grinding.

© 2010 Elsevier Ltd. All rights reserved.

Keywords: Al_2O_3; Residual stress; Spectroscopy; Fluorescence microscopy

1. Introduction

Machining is often the final stage in the fabrication of structural ceramics like alumina. It introduces near-surface damage such as cracking, grain dislodgement and plastic deformation around scratches from abrasive particles, which affects the surface integrity and the mechanical properties of the ceramic. Machining induced cracks will tend to reduce the strength, whilst compressive surface stresses from plastic deformation will tend to strengthen the material through crack closure forces. Both the cracking and the residual stresses are difficult to measure accurately so the nature of the interaction between these opposing factors remains unclear.[1–4] The work described here aims to improve the understanding of residual stresses introduced by grinding.

Previously, machining induced residual stresses in alumina and related materials have been investigated by X-ray diffraction,[5–7] curvature measurement[8] and Hertzian indentation.[9,10] The spatial resolutions of these techniques are poor,[11] both within and normal to the surface plane. Stress measurements using curvature and Hertzian indentation also require prior estimates of the thickness of the stressed layer,[8,9] which itself is difficult to measure accurately. As a result the measured stress is volume averaged rather than reflecting the local stress at the site of failure.

Confocal Cr^{3+} fluorescence microscopy, as used in this work, has higher spatial resolution (~1.5 and ~3 μm for lateral and axial resolution, respectively) than these other techniques. However, there are no reports of the use of Cr^{3+} fluorescence microscopy to investigate the residual stress in machined alumina-based ceramics to the best of the authors' knowledge, although it has been used to measure stresses induced by scratches and hardness indentations.[12–14] In order to make fully quantitative measurements, however, a major problem encountered in this previous work needs to be solved. This concerns the fact that alumina-based ceramics are translucent, and a substantial proportion of the signal therefore comes from below the

---

* Corresponding author.
** Corresponding author. Current address: Department of Mechanical Engineering, The Hong Kong Polytechnic University, Hung Hom, Kowloon, Hong Kong. Tel.: +44 1865 273718; fax: +44 1865 273783.
E-mail addresses: mmsguo@polyu.edu.hk (S. Guo), richard.todd@materials.ox.ac.uk (R.I. Todd).

0955-2219/$ – see front matter © 2010 Elsevier Ltd. All rights reserved.
doi:10.1016/j.jeurceramsoc.2010.04.016

surface. In[12,14] weakly confocal microscopes were used, which had axial (depth) resolutions approaching 10 μm (no details are available for[13]). Since grinding stresses are expected to be found at depths ∼1 μm,[9] such microscopes do not have sufficiently good resolution to make quantitative measurements on relatively transparent ceramics such as alumina. A confocal microscope with an axial resolution ∼3 μm is used in this work to alleviate this problem. However, even this resolution is not sufficient to make simple point measurements of surface stress. The measured stress is the convolution of the actual spatially distributed stresses with the probe response function (PRF)[15] describing the relative collection efficiency as a function of depth, which depends in turn on the instrument and the translucency of the material.

In the present work, the surface residual stresses after grinding and polishing in polycrystalline aluminas with different grain sizes have been measured by Cr^{3+} fluorescence microscopy, to investigate the effect of machining behavior on residual stress distribution. A model for the residual stresses simulating the displacement of material in the ground or polished condition by an array of continuously distributed edge dislocations is proposed. It is then convoluted with a PRF established previously[16,17] to compare with the experimental results. The actual residual stresses are then estimated by fitting the parameters in the stress model to the experimental results.

2. Experimental

2.1. Materials and specimen preparation

The starting powder was AKP50 alumina (200 nm, Sumitomo, Japan, 99.995% purity). 0.25 wt.% MgO was added to prevent abnormal grain growth. Mechanical mixing by attrition milling (Szegvari HD, USA) using yttria stabilized zirconia milling media was performed at a speed of 300 rpm for 2 h. The ratio of water to powder was 4:1 by volume and 2.1 wt.% of Dispex A40 (Allied Colloids, UK) was used as a dispersant. The mixture was freeze dried (Edwards Micromodulyo, UK) for 24 h. The powder was passed through a 106 μm sieve and then calcined at 600 °C for 1 h. The calcined powder was first uniaxially pressed at 50 MPa and then cold isostatically pressed at 200 MPa. Fully dense specimens were produced by pressureless sintering at maximum temperatures between 1450 and 1550 °C with a dwell time of 1–2 h. The two specimens used in this work had average grain sizes of 2.4 and 4.2 μm (Fig. 1) measured by the conventional linear intercept method.[18]

2.2. Grinding and polishing

Specimens were first sequentially polished down to a 1 μm diamond finish to start from smooth surfaces. They were first ground on a resin-bonded alumina wheel using 45 μm grit diamond spray, and then lapped using 25 μm grit diamond on another resin-alumina wheel. This was followed by 6 μm grit polishing on a resin-bonded iron wheel and then 3 μm grit polishing on a cloth. In each step, the damage induced by the previous step was removed completely. In this work, the surface residual stresses were measured in specimens in the 45 μm grit and 3 μm grit conditions, and these two machining conditions are termed *grinding* and *polishing* respectively in the following description for convenience. In these conditions, the ground or polished surfaces consist of two distinctive features (Fig. 2)[19]: (i) "ground/polished" areas, which are relatively flat and, when examined in the SEM, show scratches produced by plastic deformation of the surface[19] and (ii) "pullouts", where a piece of material has been removed from the surface by brittle fracture around its periphery. The term "pullout" in this work refers to the cavity left in the surface of the bulk specimen when a piece of material is removed, rather than the removed piece itself. The mean size (equivalent circular diameter) of the individual surface pullouts and the area fraction of pullout were measured from the optical micrographs following the procedure described previously.[19,20]

2.3. Cr^{3+} fluorescence measurements

The principle of Cr^{3+} fluorescence microscopy is to measure the stress-induced shifts of the characteristic spectral lines associated with Cr^{3+} substitutional impurities in alumina (the R1 and R2 lines, with typical positions of 14,402 and 14,432 cm^{-1}, respectively). The shift can be related to stress through the piezo-spectroscopic (PS) coefficients[12,21–25]:

$$\Delta \nu = \Pi_{ij}\sigma_{ij} \tag{1}$$

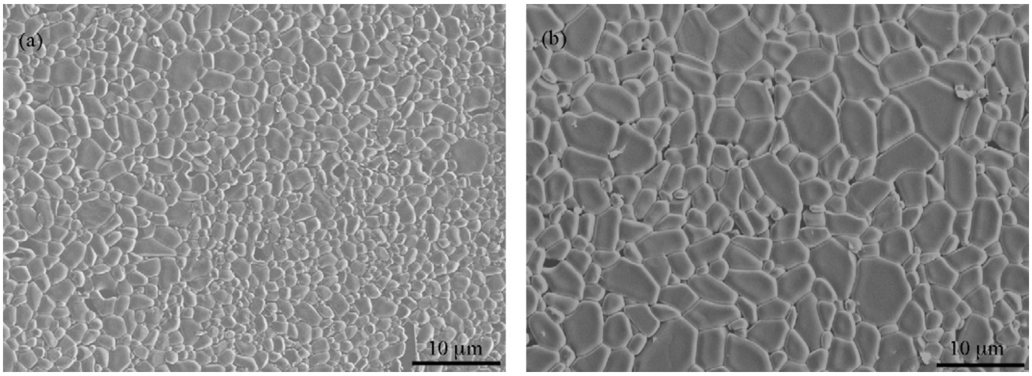

Fig. 1. Microstructure of the 2.4 μm (a) and 4.2 μm (b) sized polycrystalline aluminas used in this work. The specimens were thermally etched at 50 °C below the sintering temperature for 1 h in air to reveal the grain boundaries.

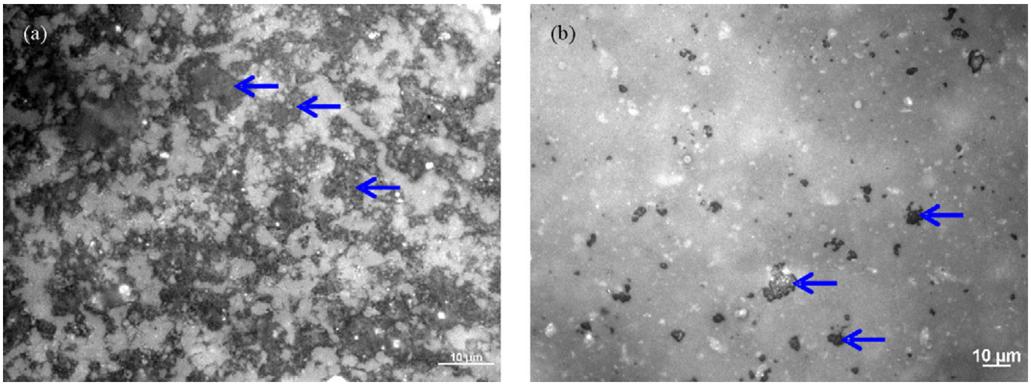

Fig. 2. Optical micrographs of machined surface of the 4.2 μm sized polycrystalline alumina. (a) After grinding and (b) after polishing. Dark regions as indicated by arrows correspond to "pullouts" and bright regions correspond to "ground" or "polished" surface.

where $\Delta\nu$ is the peak shift (cm^{-1}), σ_{ij} are the stress components (GPa) and Π_{ij} are the PS coefficients (cm^{-1} GPa^{-1}), defined in the crystallographic axial system. From Eq. (1), a positive peak shift indicates a tensile stress state, whilst a negative peak shift indicates a compressive stress state.

The fluorescence microscopy experiments were performed using a confocal Raman microscope (System 1000, Renishaw, UK) and incident radiation from a He–Ne laser at 633 nm. A 100×/0.9NA lens was used. The confocal aperture in the instrument is formed by the intersection of two slits at 90° to one another. One is a physical slit, which in the experiments described here was set to 10 μm. The other slit is virtual and is formed by using only a narrow stripe of pixels in the CCD camera used for collecting the diffraction pattern from the grating used to analyse the luminescent spectrum. The width of this stripe was set to 2 pixels in our experiments, which gives a virtual slit width corresponding to the 10 μm width of the real slit at 90° to it.

In order to measure the residual stresses, depth scans were performed through the surface of the specimen. Each scan was made through the approximate centre of either a "ground/polished" region or a "pullout" (see above). The laser was focused on the sample surface at the beginning and the sample surface at this point was defined as $z = 0$; the specimen then moved with the motorized stage so that the focus point moved from above to below the sample surface. When the probe goes into the specimen, the displacement of the sample surface relative to the focal plane, Δz, is defined to be positive. The step size was 1 μm with an exposure time of 20 s per point. The peak position and intensity were determined by fitting both R1 and R2 peaks using the mixed Lorentzian and Gaussian function (termed *two-peak fitting*) on a commercial package, Grams/32 (Galactic Industries, USA). Some spectra collected from "ground" or "polished" regions and with the focal plane (i.e. the sampling volume) close to the surface (typically within ±2 μm) could not be fitted well using two-peaks (Section 3.2); instead, an extra pair of R1 and R2 peaks was required to give a good fitting (termed *four-peak fitting*) with a constrained R1 to R2 peak area ratio (details given in Section 3.2). The four-peak fitting was carried out using an alternative fitting programme, Auto2Fit (7-D Software, China). The R1 peak position was used to characterize the peak shift, $\Delta\nu$, and the reference positions were determined from the average R1 positions (spectra collected on 20 random points) on the 1 μm polished surface of individual specimens, assumed to be residual stress free.

Section 4 describes how the stress field under the machining condition was estimated from the raw depth scan results by combining a model for the stresses with the PRF of the microscope.

3. Results

3.1. Depth scans in "pullout" regions

Typical optical micrographs of polycrystalline alumina after machining are shown in Fig. 2. "Pullouts" (dark regions in the optical micrograph) can be seen on the ground surfaces. The polished surfaces were much smoother with fewer pullouts, and the sizes of the pullouts also decreased. The measured mean pullout size and area fraction of pullout are given in Table 1.

Typical depth profiles (i.e. $\Delta\nu$ vs. Δz curves) through machined surfaces and centred on "pullout" regions, measured using two-peak fitting of the R1/R2 doublet, are given in Fig. 3.

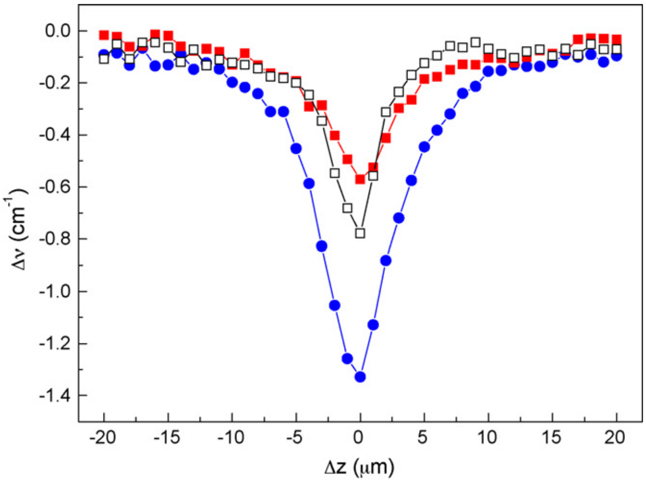

Fig. 3. Depth profiles through the pullout region for the ground 4.2 μm grain sized polycrystalline alumina. Three depth scan results measured at three different regions are shown here and the result with intermediate extent of peak shift (symbolized by "□") was used for fitting of the model as described in Section 4.

Table 1
List of the mean pullout size and area fraction of pullout for machined polycrystalline aluminas.

Average grain size, G, μm	Grinding		Polishing	
	Mean pullout size, μm	Area fraction of pullout, %	Mean pullout size, μm	Area fraction of pullout, %
2.4	6.3	54.3	2.0	1.72
4.2	8.4	50.9	2.4	2.48

$\Delta z = 0$ here is defined to be the surface at the bottom of each pullout, where the laser was initially focused (see Section 2.3). The curves exhibit a clear minimum as the optical probe passes through the surface and this was found to be the case when scanning through pullouts in both ground and polished surfaces. Examination of many regions showed that the precise extent of the peak shifts varied between individual pullouts as is evident from the examples in Fig. 3. This scattering of peak shifts due to variation in local environment was also identified for depth scan results through the "ground" or "polished" regions. For simplicity, only those results with intermediate peak R-line shifts among various depth scan results are analysed in detail in the following sections but it is noted here that the peak shift was always compressive when the optical probe was passed through the surface in a pullout and we conclude via Eq. (1) that the mean surface stress in the material beneath the pullouts was compressive.

3.2. Depth scans in "ground" or "polished" regions

Excellent fitting was obtained using two peaks for all pullout results and for most of the spectra obtained from "ground" or "polished" regions, as seen in the inset in Fig. 4(a). However, careful examination showed that spectra collected with the optical probe just below the surface in ground/polished regions could not be fitted using the two-peak fitting procedure, an example being given in Fig. 4(a). Mathematically, the fitting problem can be solved by adding another pair of R1 and R2 peaks (Fig. 4(b)), so that four peaks are used to obtain the fit. It is argued here that the two distinct doublets have a physical interpretation, with one representing the stress state within the plastically deformed layer at the surface in such regions and the other representing the elastically deformed material below it; both volumes are sampled simultaneously owing to the low axial resolution of the instrument relative to the thickness of the plastically deformed layer (see Fig. 6). However, if no constraints were imposed during four-peak fitting, the fitting results would not reflect this physical interpretation[26–28] because the extensive overlap of the two doublets makes the fitting problem mathematically ill-defined. In this work the peak area (intensity) ratios of R1 to R2 within each doublet were therefore constrained to be constant for spectra that needed the four-peak fitting treatment: $R1_A/R2_A = R1_B/R2_B = C$, where subscript A and B denote the two doublets, with A referring to the lower wavenumber doublet in what follows, and C is a constant (=2.0). The setting of this constraint was based on the fact that the intensity is almost independent of the stress[16,24,29] and the C value came from the average R1 to R2 peak area ratios for spectra collected at residual stress-free locations.[16] Comparison of the R1 and R2 peak shifts for a given doublet showed closely similar trends for both peaks, despite the severe overlap of the weaker R2 peak,[16] indicating the success of the fitting procedure in producing physically meaningful results.

The fitting results in Fig. 4(b), for a ground region of surface, were obtained using this constraint and the corresponding depth scan results of peak shift for the $R1_A$ and $R1_B$ peaks are shown in Fig. 4(c) and (d). In this particular example, only three spectra needed four-peak fitting and the results for the less intense $R1_A$ peak in Fig. 4(b) are shown for these three points in Fig. 4(c). They show large negative shifts, ranging from ~ -7.5 to $-5\,\mathrm{cm}^{-1}$. Since these overlapping peak positions are not well defined, the variation is probably due mainly to the uncertainty in the fitting, but since the shifts are large, the fractional error remains relatively small. Indeed, the relatively small scatter of the results gives confidence in the effectiveness of the constraint and the physical interpretation of the two doublets. These peak shifts indicate highly compressive stresses and can be well explained as representing the strong compressive stress expected in the plastically deformed surface layer. Fig. 4(b) also shows that the peaks of the "A" doublet are significantly broader than other peaks measured. The broadening can be associated with the dislocations and twins resulting from plastic deformation. These generate a wide range of stresses that cause peak broadening.[9] From here onwards, the $R1_A$ peaks, from the plastically deformed surface layer, will be termed *broad peaks* and $R1_B$ peaks are termed *sharp peaks*.

Fig. 4(d) shows the depth scan results for the "sharp" R1 peaks ($R1_B$) for the points where four-peak fitting was necessary, combined with the two-peak fitting results for other depths. No obvious discontinuity is observed in the points obtained from four-peak fitting. The plot shows a sharp maximum relative to the reference position ($\Delta\nu = 0$) in the ground region, indicating that the mean stress immediately beneath the assumed compressive surface layer was tensile.

Fig. 5 shows analogous broad and sharp peak depth scans for the polished specimens. The broad peak shifts again indicate a strongly compressive plastically deformed surface layer, but the plot for the sharp peaks is almost flat, showing that the stresses beneath this surface layer are small.

The essentially qualitative results above show that the surface stresses in ground and polished surfaces are highly inhomogeneous, to the extent that tensile stresses are present in some regions, notably beneath the plastically deformed surface layer of the "ground" or "polished" regions, as well as the strongly compressive stresses in other regions that are known to exist from techniques that only measure the mean stresses. A quantitative understanding of these stresses needs a more

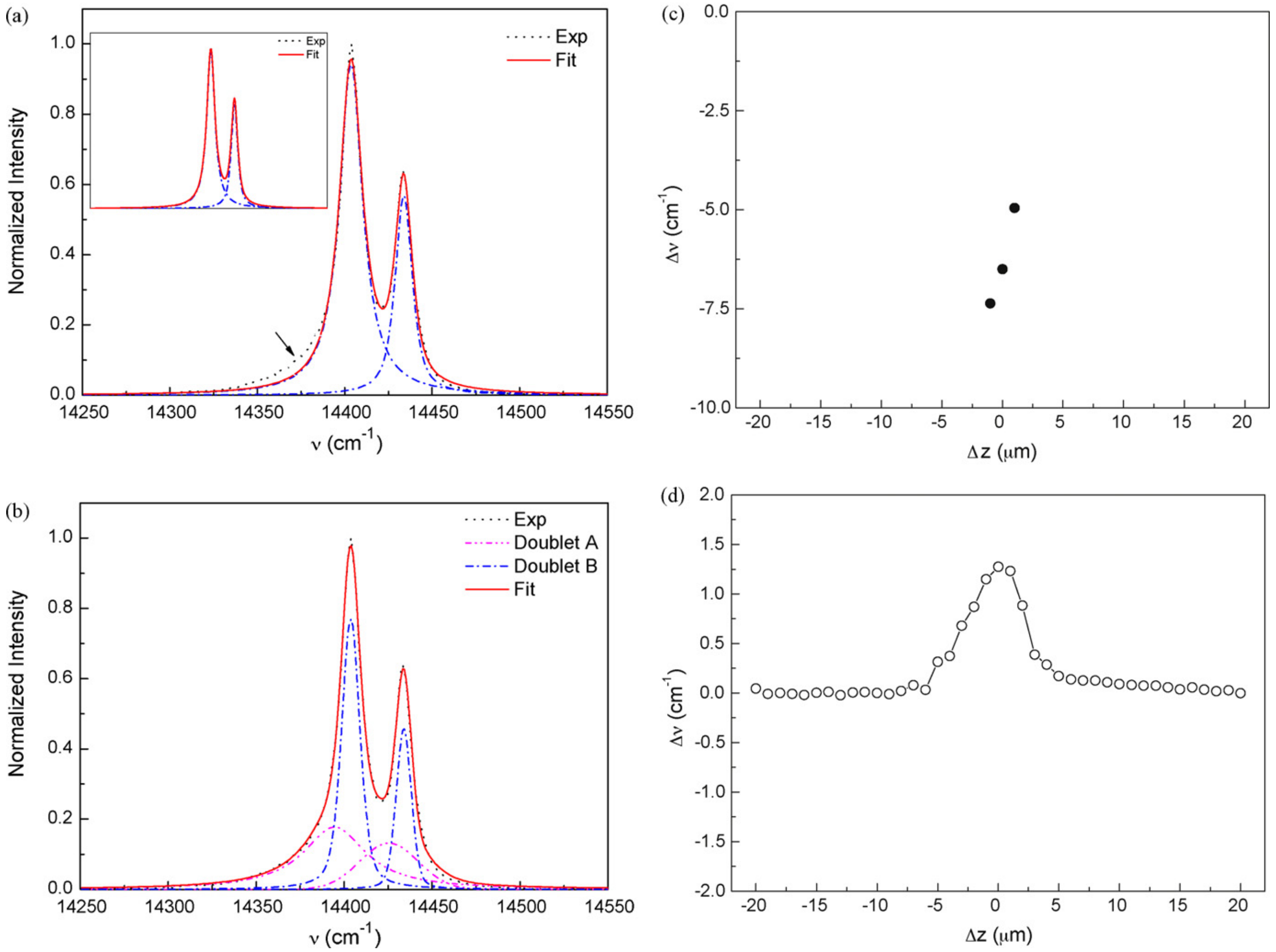

Fig. 4. (a) An example of the misfit using the two-peak fitting to fit a spectrum collected from near the ground surface, with the arrow indicating the misfit. The inset shows that two-peak fitting works well for spectra collected far away from the ground surface. (b) Improvement of curve fitting in (a) by using the four-peak fitting. (c) and (d) Show separated broad peak shifts and sharp peak shifts, respectively, from the depth profile through the ground surface of 4.2 μm sized alumina analysed using four-peak fitting where necessary.

sophisticated analysis, based on the interpretation of the results shown schematically in Fig. 6. Our approach is (i) to develop an elastic model for the near-surface stresses, (ii) to describe the sampling volume of the fluorescence microscope using its axial PRF, and (iii) to convolute the PRF with the peak shifts predicted by the stress model, adjusting the physical parameters in the model to obtain good agreement with the experimental depth scan results.

4. Modelling of stresses near ground surfaces and comparison with experiment

4.1. Model for grinding stresses

Assume the surface of the machined material is on the *xy* plane and normal to the *z* axis, as illustrated in Fig. 7(a). The machining process is thought to generate a compressed layer at the surface due to plastic deformation.[9] This compressed layer in the “ground” regions is simulated in the model by a series of continuously distributed edge dislocations with their Burgers vectors parallel to the *x* axis, line direction parallel to *y* and located at depth *d* below the surface, corresponding to the depth of plastic deformation. It is emphasised that these are fictitious dislocations whose presence is simply to model the overall deformation of the plastically deformed layer; they do not represent the real dislocations formed during the actual grinding process. For simplicity, the model assumes that the extent of plastic deformation within the ground layer is uniform.

Pullouts are represented by dislocation-free regions on the assumption that the material removed in a pullout comes from a depth sufficient to remove the entire plastically deformed layer at that point. This is supported by the fact that two-peak fitting was sufficient to give a good fit to the R1 and R2 peaks from all the spectra collected during the depth scan through the pullouts (Fig. 3), the absence of an extra “broad” doublet indicating the absence of a significant amount of plastically deformed material. In reality, pullout also creates considerable surface roughness (see Fig. 7(b)), but in the model the surface is assumed to remain flat (even at the pullouts), otherwise an analytical solution is not

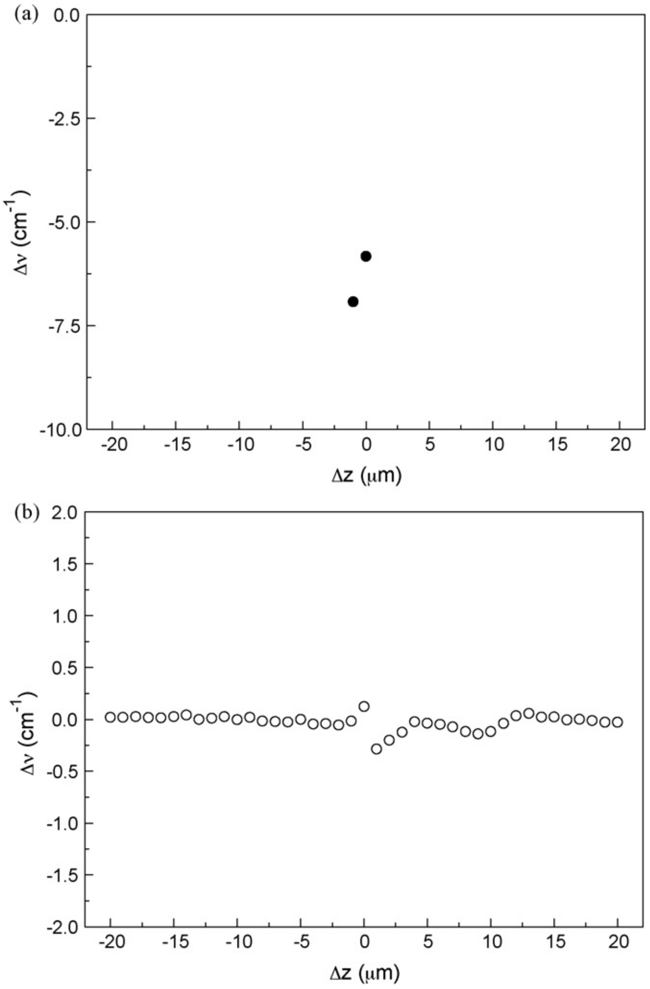

Fig. 5. Separated broad peak shifts (a) and sharp peak shifts (b) from the depth profile through the polished surface of 4.2 μm sized alumina analysed using four-peak fitting where necessary.

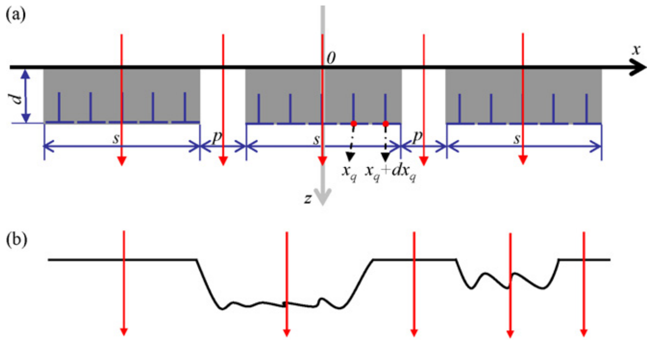

Fig. 7. (a) Schematic of islands of ground or polished surface (average size: s) and pullouts (average size: p) in the stress model. The distance between two neighbouring dislocations, dx_q, is exaggerated for clarity. The arrows across the centres of the pullout and islands of the ground/polished surface indicate the depth scan path. (b) Schematic of the real ground/polished surface and pullouts where the rough surface of the pullout and the varying size of islands of ground/polished surface and pullouts are indicated.

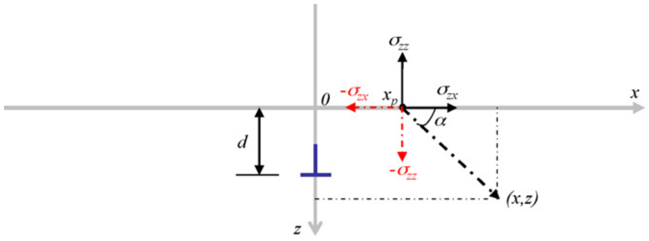

Fig. 8. Schematic showing normal and shear surface tractions at point (x_p, 0) on the free surface produced by an edge dislocation situated at (0, d).

easily derived. To simplify the problem further, all the pullouts and islands of ground or polished surface have constant sizes, p and s, respectively, and are assumed to alternate. The origin of the coordinate system is set at the surface, in the middle of an island of ground/polished surface.

It should be noted here that the model based on Fig. 7 is essentially a two-dimensional model, which might correspond well to unidirection machining damage. In our grinding and polishing, however, the machining is multidirectional because the equipment used rotates the specimen during machining. It will be shown later that fitting the experimental results to this simplified model can reasonably account for the main features of the grinding stresses but that the raw in-plane (x–y plane) stresses are overestimated. This will be discussed further in Section 5.

Derivation of the elastic stresses in the model starts from the stress field of a single edge dislocation at ($x = 0$, $z = d$) (Fig. 8). This near-surface dislocation problem has been solved previously by Atkinson et al.[30] using image forces[31] and can also be solved by the method of surface tractions.[16] Using our nomen-

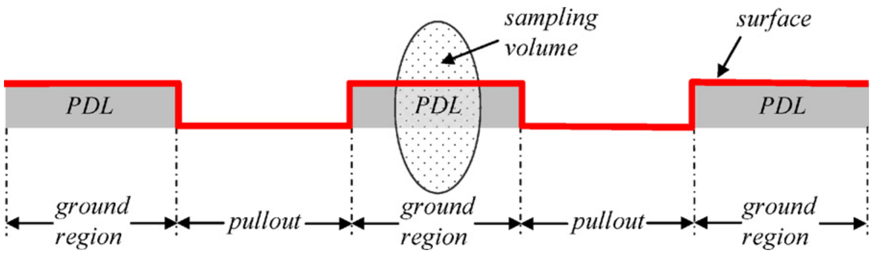

Fig. 6. Schematic of the sampling volume of the microscope during a depth scan through a ground region and the surface residual stress. *PDL* denotes plastically deformed layers, assumed to be under compression. The broad fluorescence peaks are taken to come from the intersection of the sampling volume with the PDL and the sharp peaks from the part of the sampling volume below the PDL.

clature, the stress components in the x–z plane are:

$$\sigma_{xx}(x,z) = DF(x,z,d) = D\left[\frac{(z-d)[3x^2+(z-d)^2]}{[x^2+(z-d)^2]^2} + \frac{-d[x^4-(z+d)(d^3+(d^2+6x^2)z-dz^2-z^3)]}{[x^2+(z+d)^2]^3} + \frac{[-4dx^2(d^2+x^2)-3(d^2+x^2)^2z-2d(5d^2+3x^2)z^2-4(3d^2+x^2)z^3-6dz^4-z^5]}{[x^2+(z+d)^2]^3}\right] \tag{2a}$$

$$\sigma_{zz}(x,z) = D\,G(x,z,d) = D\left[\frac{-(z-d)[x^2-(z-d)^2]}{[x^2+(z-d)^2]^2} + \frac{d[-x^4+(z+d)(d^3+5d^2z-6x^2z+7dz^2+3z^3)]}{[x^2+(z+d)^2]^3} + \frac{z[d^4-6d^2x^2+x^4+2d^3z-z^4-2d(3x^2z+z^3)]}{[x^2+(z+d)^2]^3}\right] \tag{2b}$$

$$\sigma_{zx}(x,z) = DH(x,z,d) = D\left[\frac{x[x^2-(z-d)^2]}{[x^2+(z-d)^2]^2} + \frac{2dx[x^2-3(z+d)^2]z}{[x^2+(z+d)^2]^3} + \frac{-x(-d^4+x^4+2d^3z-2dx^2z+6d^2z^2+2dz^3-z^4)}{[x^2+(z+d)^2]^3}\right] \tag{2c}$$

where $D = \mu b/2\pi(1-\nu)$, μ is the shear modulus, b, the magnitude of the Burgers vector, and ν is Poisson's ratio, taken to be 0.24 in this work.

Now consider the case of continuously distributed dislocations. At any position (x, z), the stress components σ_{xx}, σ_{zz} and σ_{zx} generated by dislocations over an elemental distance dx_q situated at $x = 0$, $z = d$ can still be described by Eq. (2), except that D in Eq. (2) becomes $D' dx_q = \mu b'/2\pi(1-\nu)\, dx_q$, where b' is the continuously distributed Burgers vector per unit length in the x direction. b' is equal to the stress-free in-plane mismatch strain between the surface layer and the bulk. Physically, it may be taken as a measure of the extent of plastic deformation in the ground layer.

Taking σ_{xx} as an example, the contribution $d\sigma_{xx}$ from the dislocations over distance dx_q situated at $(0, d)$ to σ_{xx} at any position (x, z) is:

$$d\sigma_{xx} = D' F(x,z,d)dx_q \tag{3}$$

where $F(x, z, d)$ has the same form as the right-hand side (RHS) of Eq. (2).

Similarly, the contribution of the dislocations over distance dx_q situated at (x_q, d) to σ_{xx} at (x, z) is $d\sigma_{xx} = D' F(x - x_q, z, d)\, dx_q$. Referring to Fig. 7, the contributions from all the dislocations in the array to σ_{xx} can be integrated as:

$$\sigma_{xx}(x,z) = D'\left[\int_{-s/2}^{+s/2} F(x-x_q,z,d)dx_q + \int_{s/2+p}^{3s/2+p} F(x-x_q,z,d)dx_q + \int_{-(3s/2+p)}^{-(s/2+p)} F(x-x_q,z,d)dx_q + \int_{3s/2+2p}^{5s/2+2p} F(x-x_q,z,d)dx_q + \int_{-(5s/2+2p)}^{-(3s/2+2p)} F(x-x_q,z,d)dx_q + \cdots + \int_{(2n-3)s/2+(n-1)p}^{(2n-1)s/2+(n-1)p} F(x-x_q,z,d)dx_q + \int_{-[(2n-1)s/2+(n-1)p]}^{-[(2n-3)s/2+(n-1)p]} F(x-x_q,z,d)dx_q\right] \quad (1 \le n < \infty) \tag{4a}$$

where n is the number of the pullouts.

Similarly,

$$\sigma_{zz}(x,z) = D'\left[\int_{-s/2}^{+s/2} G(x-x_q,z,d)dx_q + \int_{s/2+p}^{3s/2+p} G(x-x_q,z,d)dx_q + \int_{-(3s/2+p)}^{-(s/2+p)} G(x-x_q,z,d)dx_q + \int_{3s/2+2p}^{5s/2+2p} G(x-x_q,z,d)dx_q + \int_{-(5s/2+2p)}^{-(3s/2+2p)} G(x-x_q,z,d)dx_q + \cdots + \int_{(2n-3)s/2+(n-1)p}^{(2n-1)s/2+(n-1)p} G(x-x_q,z,d)dx_q + \int_{-[(2n-1)s/2+(n-1)p]}^{-[(2n-3)s/2+(n-1)p]} G(x-x_q,z,d)dx_q\right] \quad (1 \le n < \infty) \tag{4b}$$

Only normal stress components contribute to the peak shift in the fluorescence microscope,[12] and the model is taken to be in plane strain:

$$\sigma_{yy} = \nu(\sigma_{xx} + \sigma_{zz}) \tag{5}$$

$$\sigma_{xx} + \sigma_{yy} + \sigma_{zz} = (1+\nu)(\sigma_{xx} + \sigma_{zz}) \tag{6}$$

The predicted stress at a point is converted to a Cr^{3+} fluorescence peak shift through Eq. (1). For a randomly orientated, fine grained polycrystal subjected to a uniform stress, Eq. (1) has a simplified form[32]:

$$\begin{aligned}\Delta\nu(x,z) &= \frac{\Pi_{11}+\Pi_{22}+\Pi_{33}}{3}(\sigma_{11}+\sigma_{22}+\sigma_{33})\\ &= \frac{\Pi_{11}+\Pi_{22}+\Pi_{33}}{3}(\sigma_{xx}+\sigma_{yy}+\sigma_{zz})\\ &= 3.14(\sigma_{xx}+\sigma_{zz}) \end{aligned}\tag{7}$$

when averaged over grains of all orientations, where Π_{11}=2.56 $\mathrm{cm}^{-1}\,\mathrm{GPa}^{-1}$, Π_{22}=3.50 $\mathrm{cm}^{-1}\,\mathrm{GPa}^{-1}$ and Π_{33}=1.53 $\mathrm{cm}^{-1}\,\mathrm{GPa}^{-1}$,[23] the units of σ_{ij} are GPa and the units of $\Delta\nu$ are cm^{-1}.[23]

The depth scans through the ground or polished surface regions were assumed to pass through the centres of the islands (Fig. 7), so the predicted peak shift in the depth profile across the ground/polished surface is expressed as $\Delta\nu\ (0, z)$. This mirrors the experiments, and in any case it is shown in Section 5 that the stress variation with x is slow.

Similarly, the predicted peak shift in the depth profiles through the pullouts can be expressed as $\Delta\nu\ ((s+p)/2, z)$.

The integrals in Eqs. (4a) and (4b) were carried out numerically using the commercial software package, Mathematica (Wolfram Research, USA). $n = 100$ was used and it was proved that further increase of n had only negligible effect on the results.

In the stress model, there are four parameters characterizing the surface deformation and fracture responsible for the residual stresses, namely D', d, s and p. s and p can be experimentally determined as p can be regarded as the mean pullout size and s can be calculated from the pullout fraction: as the stress model is based on a simplified two-dimensional condition, the pullout fraction = $p/(p+s)$. D' and d are to be determined from the best fit of the model to the experimental results.

4.2. Probe response function (PRF)

In order to simulate the experimental results, it is necessary to convolute Eq. (7) with the PRF of the fluorescence microscope, taking into account the translucency of the material. We use an approach developed previously.[17]

When the laser is focused at a distance z_0 ($z_0 = n'\Delta z$, where n' is the effective refractive index[17,33]) below the surface of a translucent material such as polycrystalline alumina, the signal generated in a finite volume of material is collected, as indicated in Fig. 6. The total signal collected at depth z_0 is the integral of the fluorescence from all depths within the material[15]:

$$I(z_0) = \int_0^t g(z, z_0)\, dz \tag{8}$$

where t is the thickness of material (t can be assumed to be infinite because of the absorption that limits the probeable length) and $g(z, z_0)$ is the PRF.

Alternatively, Eq. (8) can be written as a function of sample surface displacement relative to the focal plane, Δz, in accordance with the corresponding coordinate of the depth profiles used in the experimental work as exemplified in Fig. 3:

$$I(\Delta z) = \int_0^t g(z, \Delta z)\, dz \tag{9}$$

Hence, supposing the stress field is a function of depth only, which is reasonable in this case because the depth resolution is lower than the lateral resolution and because the results of the modelling show that the variation of stress with x is slow for the locations probed,[16] the experimentally measured peak shift at depth Δz is a weighted average of the signals from all depths[15]:

$$\overline{\Delta\nu(\Delta z)} = \frac{\int_0^t \Delta\nu(z) g(z, \Delta z)\, dz}{\int_0^t g(z, \Delta z)\, dz} \tag{10}$$

where $\Delta\nu(z)$ is the real peak shift at any depth and $\overline{\Delta\nu(\Delta z)}$ is the weighted average peak shift at depth Δz, which is also the experimentally measured R-line shift in two-peak fitting.

A suitable depth resolution function, $g(z, \Delta z)$, for the present combination of instrument and material is already known from our previous work[17] and is given in Eq. (11). It captures all relevant physical effects including refraction and absorption; the scattering by pores and grain boundaries, which is important in some materials,[17] is negligible for dense polycrystalline aluminas.[16,17] Similarly, the degradation of focus when the probe is below the surface is not important for the shallow depths used here.

$$g(z, \Delta z) = e^{-2\alpha}\frac{w}{w^2 + (z - n'\Delta z)^2} \tag{11}$$

where α is the absorption coefficient and w is the probe length of the microscope. The measured parameters in Eq. (11) appropriate for our instrument and fine grained alumina are $\alpha = 0.0403\ \mu\mathrm{m}^{-1}$, $n' = 2.09$ and $w = 2.88\ \mu\mathrm{m}$, respectively.[17] It agrees very well with the experimentally measured intensity vs. depth profiles as seen in Fig. 9.

4.3. Convolution and fitting to experimental depth scans

The R1 fluorescence peaks shifts predicted by the model may be obtained by the convolution in Eq. (10) over appropriate limits. There are three cases. For the broad peaks corresponding to the stress state within the plastically deformed surface layer in “ground” or “polished” regions, the peak shift during a depth scan is given by:

$$\overline{\Delta\nu(\Delta z)} = \frac{\int_0^d \Delta\nu(0, z) g(z, \Delta z)\, dz}{\int_0^d g(z, \Delta z)\, dz} \tag{12}$$

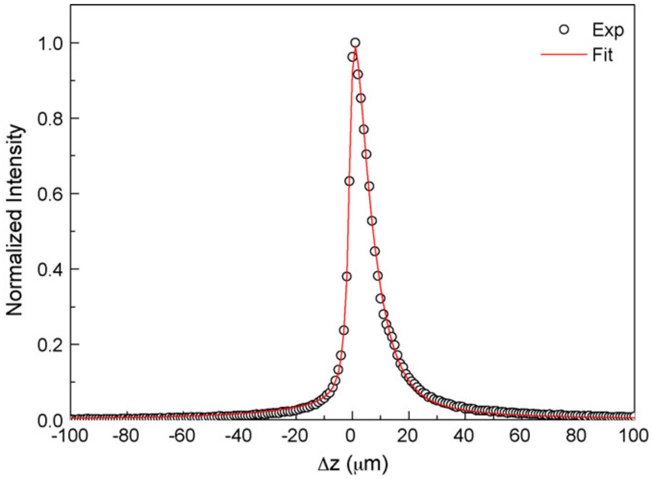

Fig. 9. Fitting of the PRF model based on Eq. (11) to the experimental data of intensity vs. depth for polycrystalline alumina.

For the sharp peaks in "ground" or "polished" regions the convolution is:

$$\overline{\Delta\nu(\Delta z)} = \frac{\int_d^t \Delta\nu(0, z)g(z, \Delta z)\,dz}{\int_d^t g(z, \Delta z)\,dz} \tag{13}$$

Similarly, for the depth profiles through the pullouts, the predicted peak shift follows:

$$\overline{\Delta\nu(\Delta z)} = \frac{\int_0^t \Delta\nu((s+p)/2, z)g(z, \Delta z)\,dz}{\int_0^t g(z, \Delta z)\,dz} \tag{14}$$

Eqs. (12) and (13) were then used with the experimentally measured values of s and p to fit the broad peak and sharp peak shifts obtained in the depth profiles through ground/polished surfaces as exemplified in Fig. 4(c) and (d), respectively, by varying D' and d to reach a compromise best fit for both. Only results with the focal plane at or beneath the surface were used; when the focal plane is above the surface, the signal obtained comes from one of the tails of the PRF and this is not accurately modelled by Eq. (11). Typical fitting results are shown in Fig. 10(a) and (b). The agreement is excellent considering (i) the idealised nature of the model and (ii) the fact that there are only two adjustable parameters, both with clear physical meaning. It is immediately apparent from Fig. 10(b) that the model successfully predicts the presence of tensile stresses beneath the surface.

The fitted values of D' and d were then used to predict the depth profiles through the pullouts with no further adjustment of parameters. The example in Fig. 10(c) shows that the model successfully predicts the presence of compressive stresses beneath the pullouts and the approximate extent of their depth below the surface. The predicted peak shift is of the correct order of magnitude and spatial extent but is greater than was measured experimentally by about a factor of 2. One reason for this discrepancy is undoubtedly the simplicity of the stress model, and another is that the in-plane resolution of the microscope is not much less than the pullout dimensions, so that less highly stressed material around the centre line of an individual pullout is included in the experimental measurement. A further, systematic source of error is that the s and p used in predicting the residual stress in Fig. 10(c) using Eqs. (12)–(14) are the *average* values measured from the optical micrographs; they do not necessarily represent the local environment where the depth scans were actually made. In the real depth scans through pullouts, larger pullouts (larger p) were chosen for examination as they were easier to identify under the microscope. The model shows that larger values of p give lower stresses beneath pullouts, as observed, and it was found that the fit in Fig. 10(c) could be improved substantially, whilst maintaining a good fit in the ground/polished regions, by increasing p/s.[16] Whilst quantitative prediction of the precise stress field in an individual pullout is evidently too sensitive to local environment to be very accurate, we conclude that the model captures the essential features of the residual stresses. The values of D' and d obtained from depth scans through the "ground" or "polished" regions of the surface were not very sensitive to p/s for realistic conditions,[16] so these fitted values are robust.

The fitted values of D' and d for different surface treatments and grain sizes are listed in Table 2. It is worth pointing out that although these D' and d values came from fitting results for depth scans of a single area in both cases, the results chosen for this detailed analysis were representative, i.e. with intermediate peak R-line shifts among various depth scan results; hence these fitted D' and d values should also be representative. To give some confidence, the scattering for D' and d is within 20 and 35%, respectively, based on their values determined from multiple experiments (depth scans made at various locations). D', representing the extent of plastic deformation, is not sensitive to grain size and is smaller in polishing than in grinding. The major difference between grinding and polishing, however, is that the depth of plastic deformation is much less in polishing than in grinding.

5. Discussion

By substituting D', d, s and p listed in Table 2 into Eqs. (4a) and (4b), the stress distributions predicted by the optimised model can be calculated. Caution has to be taken with the raw values for the in-plane stresses (σ_{xx}) calculated in this way, recalling the two-dimensional simplification of the grinding stress model (Section 4.1). A plane strain state was assumed in the model where $\varepsilon_{yy} = 0$ and $\sigma_{yy} = \nu\sigma_{xx}$. The situation in our grinding treatment actually has biaxial symmetry in the surface plane. Assuming the true in-plane stresses are $\sigma_{xx} = \sigma_{yy} = \sigma_t$, σ_t can be estimated by equalizing the total normal stresses that determine the peak shift in the two conditions: $2\sigma_t = (1+\nu)\sigma_{xx}$ and hence $\sigma_t = (1+\nu)\sigma_{xx}/2 = 0.62\sigma_{xx}$. It is thus evident that the raw σ_{xx} results overestimate the true in-plane stresses by a factor of ~1.6 when fitted to the biaxial experimental results. The true values for the in-plane stresses, σ_t, estimated as $0.62\sigma_{xx}$, are listed in Table 3, which shows the extremes of tensile and compressive stresses (both raw and adjusted results) obtained from the plane strain model. The out-of-plane stresses, σ_{zz}, are expected to be affected less by this consideration as they arise from the sum of contributions in the notional grinding directions and so are insensitive to the relative contributions to the shift from the x and y directions. Obviously the fitting procedure is

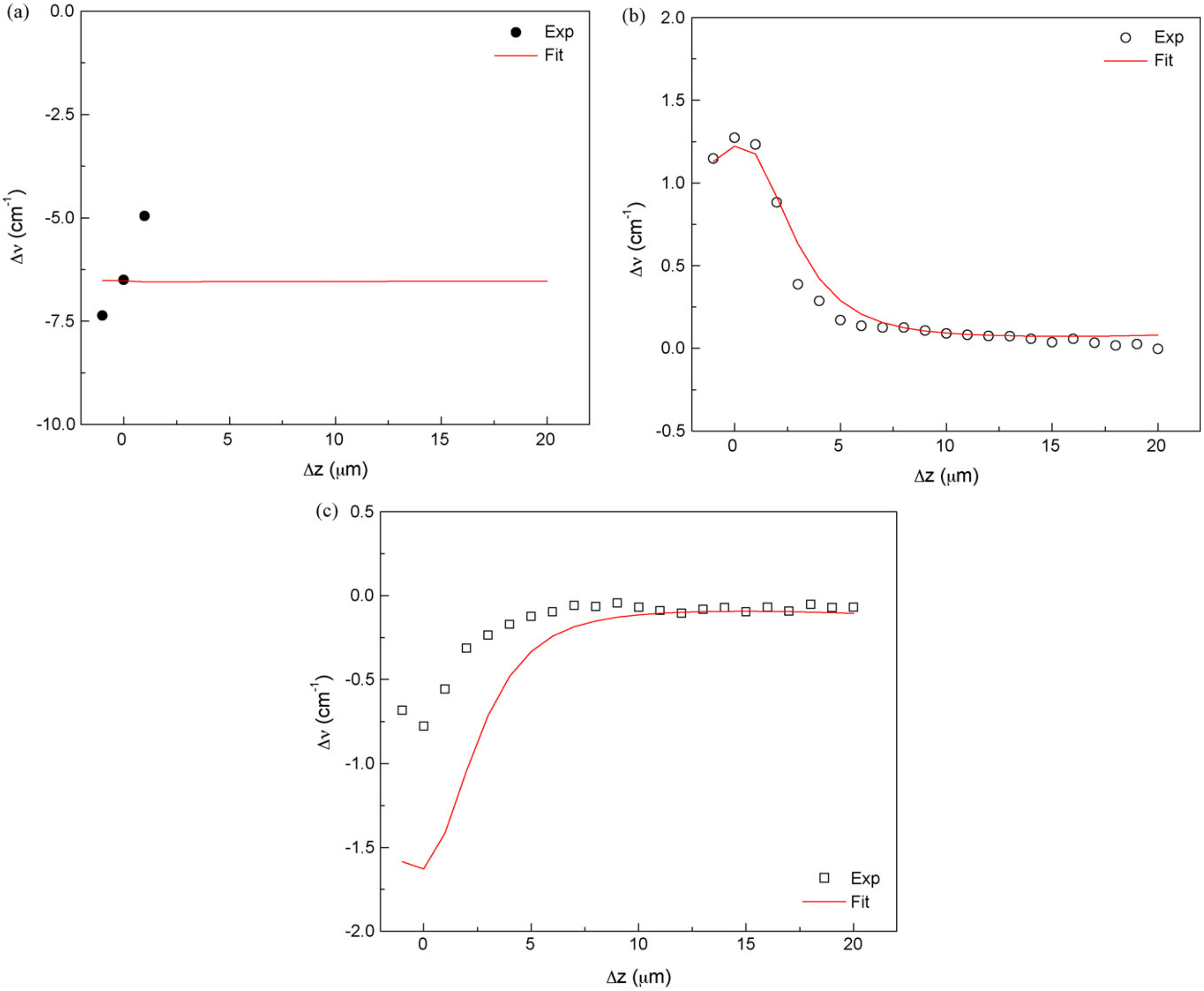

Fig. 10. Fitting results of Eqs. (12)–(14) to depth profiles of the 4.2 μm sized ground polycrystalline alumina. (a) and (b) Broad peak shifts and sharp peak shifts from the ground surface, respectively; (c) peak shifts from the pullout.

also affected by these considerations in principle, but in practice the overall stress level is dictated by the "broad" peaks from the plastically deformed surface layer and the shape of the curves will be affected by similar considerations in plane strain and biaxial symmetry (thickness of deformed layer, relative sizes of pullouts and "ground" regions, by St. Venant's principle) so it is likely that the consequences are minor.

Despite this difficulty with the plane strain model, all stresses within it are expected to be within a factor of 2 of the true values and the distributions of stress it reveals are very informative. Typical plots of the spatial distribution of the stress components are shown in Fig. 11. In view of the universal conclusion of previous works measuring mean surface stresses that these are compressive, an interesting conclusion of the present local stress measurements is that in all the ground specimens, σ_{xx} and σ_{zz} fluctuate to such an extent that they are strongly tensile for some distance below the plastically deformed "ground" regions of the surface. The maximum tensile stresses in the ground condition are $\sigma_{xx} \sim 1$ GPa ($\sigma_t \sim 600$ MPa) and $\sigma_{zz} \sim 250$ MPa, respectively (Table 3). This is very important in explaining the

Table 2
D', d, s and p for ground and polished polycrystalline alumina. D' and d are from the best fit of the model to the experimental results; s and p are measured directly from optical micrographs.

G (μm)	Grinding				Polishing			
	D' (GPa)	d (μm)	s (μm)	p (μm)	D' (GPa)	d (μm)	s (μm)	p (μm)
2.4	0.28	1.34	5.3	6.3	0.19	0.25	114.5	2.0
4.2	0.23	1.32	8.1	8.4	0.17	0.66	94.5	2.4

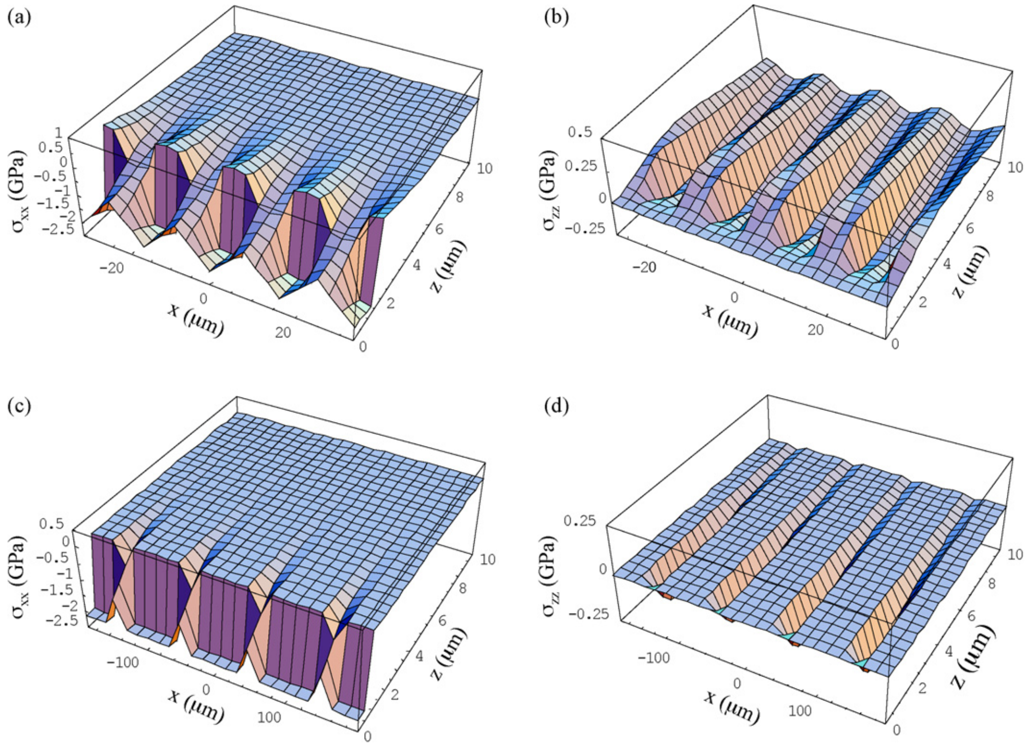

Fig. 11. Stress distribution in the ground and polished 4.2 μm sized polycrystalline alumina in a two-dimensional view. (a) σ_{xx} for ground specimen; (b) σ_{zz} for ground specimen; (c) σ_{xx} for polished specimen; (d) σ_{zz} for polished specimen. The surface is at $z = 0$ and $x = 0$ corresponds to the centre of a ground/polished region of the surface. The σ_{xx} values in (a) are based on the 2D model in Fig. 7 and estimated values for the in-plane stresses in the biaxial condition of the experiments (σ_t) are listed in Table 3.

cracking behavior in grinding: tensile σ_{xx} will lead to crack growth normal to the surface if it is beyond the fracture strength of the material, and tensile σ_{zz} will lead to material spalling off and grain pullout. There are no tensile stresses in the model if pullouts are not introduced,[16] and neither were they observed experimentally in the polished specimens (Fig. 5), where the amount of pullout is small. There are two important conclusions to draw from this. First, although more severe grinding leads to a greater *mean* compressive surface stress, which has previously been seen as a strengthening mechanism,[6,8,34] its potential benefits are severely compromised not only by the cracks nucleated by grinding, but also by the appearance of local tensile stresses in some regions which act to help such cracks to grow. Secondly, once pullouts start to form by surface fracture, it becomes easier to form further pullouts owing to the increasingly tensile stress normal to the surface and just below the plastically deformed layer. This "positive feedback" will be expected to lead to instability and may play an important part in the sudden and catastrophic transition from mild to severe wear often observed after some time in sliding wear tests.

Both ground and polished surfaces also contain very strong in-plane compressive stresses ($\sigma_t \sim -1.5$ GPa) in the plastically deformed layer (Table 3). It is difficult to compare these directly with other works in which stresses have been measured by the curvature method,[8] X-ray diffraction[5–7] or Hertzian indentation[9,10] because of the different grinding and polishing treatments used but the maximum compressive residual stresses obtained in this work are at the high end of the ranges reported using other methods (ranging from ~ -50 MPa to -1.5 GPa). One reason for the high values is that the residual stresses obtained in this work are not volume averaged and reflect the local stress at different points in the stressed surface layer. The maximum compressive stress in the plastically deformed layer is similar in the ground and polished conditions. Table 2 shows that D', which indicates the severity of plastic deformation in the plastically deformed layer, is actually ∼40% greater in the ground condition, but the effect of this on the compressive stress is offset by relaxation caused by the greater amount of pullout in the ground specimens compared with the polished condition.

The main difference between the ground and polished conditions is in the depth of the plastic deformation, d (Table 2), which was about three times greater after grinding than it was after polishing. The magnitude of d for both grinding and polishing conditions are in good agreement with transmission electron microscopy (TEM) observations of the depth to which severe plastic deformation is observed following typical surface treatments.[9]

This work therefore suggests two explanations for the success of polishing treatments in avoiding surface fracture. The first is that the lower intensity (D') and depth of plastic deformation, and therefore the lesser intensity and length of stress concentrators such as twins and dislocation pileups, reduces the rate at which brittle fracture is nucleated. The second is that the reduction in depth and intensity of plastic deformation generates smaller tensile stresses when the pullouts are formed and thus helps to avoid the avalanche effect described above.

Table 3
List of maximum tensile and compressive stresses in ground or polished surface and pullouts for the two polycrystalline aluminas as obtained from the 2D model in Fig. 7. Both raw (σ_{xx}) and true (σ_t) in-plane stresses are listed.

	G (μm)	Ground region ($x=0$)					Pullout region ($x=(s+p)/2$)		
		σ_{xx} (t_{max}[a]) (GPa)	σ_t (t_{max}) (GPa)	σ_{xx} (c_{max}[b]) (GPa)	σ_t (c_{max}) (GPa)	σ_{zz} (t_{max}) (GPa)	σ_{xx} (c_{max}) (GPa)	σ_t (c_{max}) (GPa)	σ_{zz} (c_{max}) (GPa)
Grinding	2.4	0.94	0.58	−2.58	−1.60	0.27	−1.23	−0.76	−0.23
	4.2	0.66	0.41	−2.23	−1.38	0.18	−0.83	−0.51	−0.17
Polishing	2.4	0	0.00	−2.39	−1.48	0	−0.73	−0.45	−0.14
	4.2	0	0.00	−2.13	−1.32	0	−1.26	−0.78	−0.20

[a] Maximum tensile stresses.
[b] Maximum compressive stresses.

The stress state in the material beneath the pullouts is strongly compressive ($\sigma_t = -450$ to -750 MPa) and there was little difference between the levels of stress following grinding and polishing. This is a trade off between there being a greater area of unspalled, plastically deformed surface surrounding the pullouts in the polished condition but a lower level of plastic deformation in this surrounding area.

The grain size had no obvious effect on the results. The pullouts were larger in the coarser grained material, as expected from the intergranular fracture mode[19] although it is surprising that this did not lead to a greater area fraction of pullout (Table 1). This may be a result of the difficulty of reproducing surface treatment conditions from one run to the next.[8]

6. Summary

Local residual stress distributions in ground and polished surfaces of alumina have been measured using Cr^{3+} fluorescence microscopy. To analyse the results, a model for the residual stresses simulating the displacement of material in the ground or polished condition by an array of continuously distributed edge dislocations has been proposed. It was convoluted with a probe response function established previously to compare with the nominal residual stresses experimentally measured by Cr^{3+} fluorescence microscopy. By fitting the model to the experimental results, the magnitude and spatial distribution of the residual stresses was obtained. Interestingly, large tensile stresses both parallel (~600 MPa) and normal (~250 MPa) to the surface were found for some distance below unfractured surface regions of coarsely ground specimens. These would aid crack growth and the spallation of material to cause grain pullout during grinding. The tensile stresses occur only in the presence of pullouts and existing pullouts will therefore facilitate further pullout formation. The compressive stresses in the ground and polished surfaces were similar (~ -1.5 GPa) and were greater than the mean stresses measured by other, low spatial resolution methods but the depth of plastic deformation after grinding (~1.3 μm) was about three times greater than that for polishing (~0.4 μm).

Acknowledgements

S Guo would like to thank the K C Wong Education Foundation and the Overseas Research Students Awards Scheme for the financial support to his D.Phil study at University of Oxford.

References

1. Sakaida Y, Tanaka K. Effect of grinding method on bending strength of silicon nitride. *JSME International Journal Series A-Solid Mechanics and Material Engineering* 1999;**42**:560.
2. Rao MP, Lange FF. Factors affecting threshold strength in laminar ceramics containing thin compressive layers. *Journal of the American Ceramic Society* 2002;**85**:1222.
3. Tandon R, Green DJ. Crack stability and T-curves due to macroscopic residual compressive stress profiles. *Journal of the American Ceramic Society* 1991;**74**:1981.
4. Tandon R, Green DJ. The effect of crack-growth stability induced by residual compressive stresses on strength variability. *Journal of Materials Research* 1992;**7**:765.

5. Lange FF, James MR, Green DJ. Determination of residual surface stresses caused by grinding in polycrystalline Al_2O_3. *Journal of the American Ceramic Society* 1983;**66**:C16.
6. Tanner BK, Wu HZ, Roberts SG. Direct evidence for compressive elastic strain at ground surfaces of nanocomposite ceramics. *Applied Physics Letters* 2005:86.
7. Tanner BK, Wu HZ, Roberts SG, Hase TPA. Subsurface damage in alumina and alumina–silicon carbide nanocomposites. *Philosophical Magazine* 2004;**84**:1219.
8. Chou IA, Chan HM, Harmer MP. Machining-induced surface residual stress behavior in Al_2O_3–SiC nanocomposites. *Journal of the American Ceramic Society* 1996;**79**:2403.
9. Wu H, Roberts SG, Derby B. Residual stress and subsurface damage in machined alumina and alumina/silicon carbide nanocomposite ceramics. *Acta Materialia* 2001;**49**:507.
10. Wu HZ, Lawrence CW, Roberts SG, Derby B. The strength of Al_2O_3/SiC nanocomposites after grinding and annealing. *Acta Materialia* 1998;**46**:3839.
11. Withers PJ, Turski M, Edwards L, Bouchard PJ, Buttle DJ. Recent advances in residual stress measurement. *International Journal of Pressure Vessels and Piping* 2008;**85**:118.
12. Molis SE, Clarke DR. Measurement of stresses using fluorescence in an optical microprobe: stresses around indentations in a chromium-doped sapphire. *Journal of the American Ceramic Society* 1990;**73**: 3189.
13. Banini GK, Chaudhri MM, Smith T, Hayward IP. Measurement of residual stresses around Vickers indentations in a ruby crystal using a Raman luminescence microscope. *Journal of Physics D-Applied Physics* 2001;**34**:L122.
14. Wu HZ, Roberts SG, Derby B. Residual stress distributions around indentations and scratches in polycrystalline Al_2O_3 and Al_2O_3/SiC nanocomposites measured using fluorescence probes. *Acta Materialia* 2008;**56**:140.
15. Ma Q, Clarke DR. Measurement of residual stresses in sapphire fiber composites using optical fluorescence. *Acta Metallurgica et Materialia* 1993;**41**:1817.
16. Guo S. Fluorescence Microscopy Investigation on Residual Stresses in Alumina-based Ceramics, PhD Thesis. University of Oxford; 2009.
17. Guo S, Todd RI. Confocal fluorescence microscopy in alumina-based ceramics: where does the signal come from? *Journal of the European Ceramic Society* 2010;**30**:641.
18. Wurst JC, Nelson JA. Linear intercept technique for measuring grain-size in a 2-phase polycrystalline ceramics. *Journal of the American Ceramic Society* 1972;**55**:109.
19. Ortiz-Merino JL, Todd RI. Relationship between wear rate, surface pullout and microstructure during abrasive wear of alumina and alumina/SiC nanocomposites. *Acta Materialia* 2005;**53**: 3345.
20. Limpichaipanit A, Todd RI. The relationship between microstructure, fracture and abrasive wear in Al_2O_3/SiC nanocomposites and microcomposites containing 5 and 10% SiC. *Journal of European Ceramic Society* 2009;**29**:2841.
21. Ma Q, Clarke DR. Optical fluorescence from chromium ions in sapphire—a probe of the image stress. *Acta Metallurgica et Materialia* 1993;**41**:1811.
22. Grabner L. Spectroscopic technique for measurement of residual-stress in sintered Al_2O_3. *Journal of Applied Physics* 1978;**49**:580.
23. He J, Clarke DR. Determination of the piezospectroscopic coefficients for chromium-doped sapphire. *Journal of the American Ceramic Society* 1995;**78**:1347.
24. He J, Clarke DR. Polarization dependence of the Cr^{3+} R-line fluorescence from sapphire and its application to crystal orientation and piezospectroscopic measurement. *Journal of the American Ceramic Society* 1997;**80**:69.
25. Eggert JH, Goettel KA, Silvera IF. Ruby at high pressure. 1. Optical line shifts to 156 GPa. *Physical Review B* 1989;**40**:5724.
26. Nychka JA, Clarke DR. Damage quantification in TBCs by photo-stimulated luminescence spectroscopy. *Surface & Coatings Technology* 2001;**146**:110.
27. Selcuk A, Atkinson A. Analysis of the Cr^{3+} luminescence spectra from thermally grown oxide in thermal barrier coatings. *Materials Science and Engineering A-Structural Materials Properties Microstructure and Processing* 2002;**335**:147.
28. Wang X, Atkinson A. Piezo-spectroscopic mapping of the thermally grown oxide in thermal barrier coatings. *Materials Science and Engineering A-Structural Materials Properties Microstructure and Processing* 2007;**465**:49.
29. Munro RG, Piermarini GJ, Block S, Holzapfel WB. Model line-shape analysis for the ruby R lines used for pressure measurement. *Journal of Applied Physics* 1985;**57**:165.
30. Atkinson A, Jain SC, Harker AH. Strain, dislocations, and critical dimensions of laterally small lattice-mismatched semiconductor layers. *Journal of Applied Physics* 1995;**77**:1907.
31. Hull D, Bacon DJ. *Introduction to dislocations*. fourth edition Oxford: Butterworth-Heinemann; 2001.
32. Ma Q, Clarke DR. Stress measurement in single-crystal and polycrystalline ceramics using their optical fluorescence. *Journal of the American Ceramic Society* 1993;**76**:1433.
33. Everall NJ. Modeling and measuring the effect of refraction on the depth resolution of confocal Raman microscopy. *Applied Spectroscopy* 2000;**54**:773.
34. Zhao J, Stearns LC, Harmer MP, Chan HM, Miller GA. Mechanical behavior of alumina–silicon carbide nanocomposites. *Journal of the American Ceramic Society* 1993;**76**:503.